

Breaking into the window of primordial black hole dark matter with x-ray microlensing

Manish Tamta¹,* Nirmal Raj¹,† and Prateek Sharma¹,‡
Indian Institute of Science, C. V. Raman Avenue, Bengaluru 560012, India
 (Dated: June 3, 2024)

Primordial black holes (PBHs) in the mass range $10^{-16} - 10^{-11} M_{\odot}$ may constitute all the dark matter. We show that gravitational microlensing of bright x-ray pulsars provide the most robust and immediately implementable opportunity to uncover PBH dark matter in this mass window. As proofs of concept, we show that the currently operational NICER telescope can probe this window near $10^{-14} M_{\odot}$ with just two months of exposure on the x-ray pulsar SMC-X1, and that the forthcoming STROBE-X telescope can probe complementary regions in only a few weeks. These times are much shorter than the year-long exposures obtained by NICER on some individual sources. We take into account the effects of wave optics and the finite extent of the source, which become important for the mass range of our PBHs. We also provide a spectral diagnostic to distinguish microlensing from transient background events and to broadly mark the PBH mass if true microlensing events are observed. In light of the powerful science case, i.e., the imminent discovery of dark matter searchable over multiple decades of PBH masses with achievable exposures, we strongly urge the commission of a dedicated large broadband telescope for x-ray microlensing. We derive the microlensing reach of such a telescope by assuming sensitivities of detector components of proposed missions, and find that with hard x-ray pulsar sources PBH masses down to a few $10^{-17} M_{\odot}$ can be probed.

I. INTRODUCTION

One appealing contender for the make-up of the unidentified dark matter is primordial black holes (PBHs), formed likely due to density perturbations generated during the inflationary epoch of the universe [1, 2].

Hunted extensively by looking for signatures of their evaporation, gravitational microlensing, accretion-induced distortion of the relic radiation, gravitational waves from binary mergers, and dynamical effects in stellar systems, they have left open a mass window between about $10^{-16} - 10^{-11} M_{\odot}$ over which they can constitute 100% of the dark matter; see Ref. [2] for the most up-to-date constraints. In this paper we show that gravitational microlensing performed at current and imminent x-ray telescopes can, for the very first time, realistically probe this mass window. Our main result is shown in Figure 1, which we will discuss in detail in Sec. III.2.

Microlensing is the temporary magnification of a background star due to the gravitational field of a transiting body, with images typically unresolved. It is a technique that, using stellar sources in the Milky Way and neighbouring galaxies, has ruled out massive compact halo objects (MACHOs) and PBHs in the mass range from $10^{-11} - 10 M_{\odot}$ as the entire content of dark matter [4]. The technique can also be applied, albeit in a non-trivial way, to extended objects with various density distributions [4–10]. The smallest PBH masses reached by microlensing were constrained by the Subaru-HSC instrument [4, 11, 12], which was sensitive to the short transit

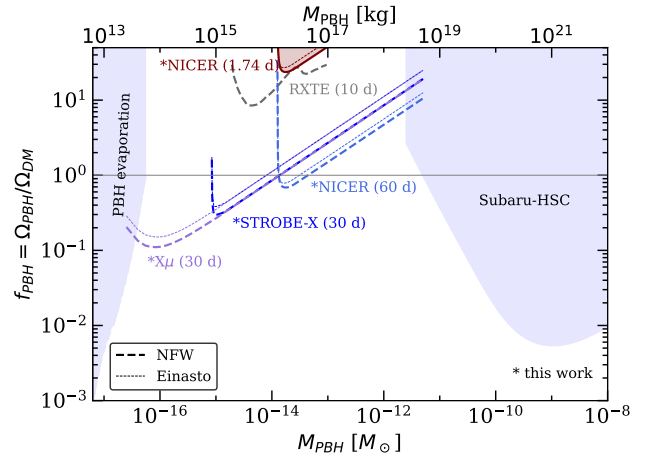


FIG. 1. 90% C.L. constraints on primordial black hole dark matter from observations of the x-ray pulsar SMC X-1 over 1.74 days at NICER, and projected reaches of NICER (60 days on SMC-X1), the future STROBE-X (30 days on SMC-X1), and our proposed $X\mu$ (30 days on a Crab-like hard x-ray pulsar in the SMC). With one year of exposure at NICER, as obtained for other individual sources, f_{PBH} about six times smaller than the 60-day reach shown here can be constrained. Also shown are x-ray microlensing limits using RXTE [3], optical microlensing using Subaru-HSC [4], and PBH evaporation [2]. See Sec. III.2 for further details.

times of light PBHs. However, the Subaru-HSC survey was limited by the twin effects of [i] the finite apparent size of the source stars in its sky target, M31, being larger than the apparent Einstein radius, yielding poorly focused light, and [ii] transition from geometric to wave optics as the PBH Schwarzschild radius becomes comparable to or smaller than the wavelength of optical light as

* manishtamta@iisc.ac.in

† nraj@iisc.ac.in

‡ prateek@iisc.ac.in

the PBH mass is reduced. Therefore, broadly speaking, to probe PBH masses less than $10^{-11} M_\odot$ one must seek to microlens compact sources that emit in wavelengths smaller than optical. Reference [3] recognized that accreting x-ray pulsars in the Magellanic Clouds provide just such a source, which moreover furnish a steady flux above which transient magnification of microlensing can be discerned, and are located far enough from Earth to provide appreciable optical depth of intervening PBHs. In that work, limits on atom-sized PBHs were derived from 10 days of observations at the Rossi X-ray Timing Explorer (RXTE) satellite on x-ray pulsars in the Magellanic Clouds, but these could only exclude the unphysical scenario of PBH densities higher than that of dark matter. Future projections of such other satellites as eXTP, AstroSat, Lynx, and Athena with 300 days of exposure were shown to be more promising.

In this work, we will show that the ongoing Neutron Star Interior Composition Explorer Mission (NICER), designed primarily to measure the masses and radii of accreting x-ray pulsars, can constrain PBHs in the mass window as a physical fraction of the dark matter population with merely two months of live exposure. This is smaller than or comparable to the exposure already obtained by NICER on multiple sources. Moreover, the future STROBE-X satellite, touted as the spiritual successor of NICER, would require even less exposure for this purpose thanks to its much larger effective area and wider coverage of x-ray frequencies. We estimate the reaches of these telescopes as a proof of concept that the observation of bright x-ray pulsars provide our best opportunity to discover dark matter in the PBH mass window of $10^{-16} - 10^{-11} M_\odot$. One main message of our paper is that *the science case is strong enough to fly a dedicated x-ray satellite for microlensing*. Such a telescope should have a large effective area of about 1–10 m² and operate in the 0.1–1000 keV energy range, achievable traits as seen in the designs of the proposed instruments STROBE-X [13], LOFT-P [14] and Daksha [15]. It should also continuously observe source candidates for a few weeks or months. The costs of such a campaign are completely warranted given the monumental nature of discovering dark matter in an untouched region spanning five orders of magnitude. In the rest of the paper, we will call this hypothetical future telescope “X μ ”, a name to connote x-ray microlensing.

This paper is laid out as follows. In Section II we review the framework of gravitational microlensing by point-like lenses, with emphasis on x-ray pulsar sources and the effects of wave optics and finite source. Here we discuss the identification of microlensing-induced magnification in the photon count rate data obtained at x-ray telescopes, and provide a diagnostic for distinguishing microlensing events from transient backgrounds, namely, the inspection of photon frequency data. In Section III we derive event rates and summarize our prescription for setting microlensing limits in x-ray telescopes, using which we obtain limits on the population of PBHs with

currently available NICER data, and future reaches of NICER, STROBE-X and X μ . In Section IV we provide discussion on the scope of our study. In the appendix we provide some background material for key formulae used in the paper, and briefly survey alternative ideas in the literature for probing the PBH mass window. We generally use natural units, $\hbar = c = 1$, but in some expressions we will restore \hbar and c for clarity.

II. X-RAY MICROLENSING

II.1. Basic set-up

The geometric set-up of microlensing is illustrated in, e.g., Refs. [4, 8, 16], and microlensing of x-ray pulsars has been described in detail in Ref. [3]. Here we briefly review the essentials, consigning to Appendix A derivations of formulae.

Defining $x \equiv D_L/D_S$ as the ratio of the observer-lens distance D_L to observer-source distance D_S , the Einstein radius for a point-like lens of mass M is given by

$$\begin{aligned} r_E &= \sqrt{\frac{4GMx(1-x)D_S}{c^2}} \\ &= 54 \text{ km} \left[\left(\frac{M}{10^{-15} M_\odot} \right) \left(\frac{D_S}{65 \text{ kpc}} \right) \left(\frac{x(1-x)}{0.25} \right) \right]^{1/2}. \end{aligned} \quad (1)$$

This quantity is the closest distance that source photons get to the lens when it lies directly along the line of sight. As line-of-sight distances of interest are generally much greater than transverse distances in the problem, microlensing events may be visualized as projections on the lens-containing transverse plane, the “lens plane”. It then becomes useful to express distances in units of r_E . The source radius in the lens plane is $a_S(x) \equiv xR_S/r_E$, and (in units of r_E) the distance from the lens center to the source center (i.e., the impact parameter) is y . As a function of these quantities, the magnification obtained at a telescope averaged over the energy range $[E_{\min}, E_{\max}]$, weighted by the spectral energy distribution (SED) of the source $\mathcal{F}(E)$ and the energy-dependent effective area of the telescope $\mathcal{A}(E)$ is

$$\bar{\mu}_E(y, a_S(x)) = \frac{\int_{E_{\min}}^{E_{\max}} dE \mathcal{A}(E) \mathcal{F}(E) \mu(w, y, a_S(x))}{\int_{E_{\min}}^{E_{\max}} dE \mathcal{A}(E) \mathcal{F}(E)}, \quad (2)$$

where

$$\begin{aligned} \mu(w, y, a_S(x)) &= a_S^{-2} e^{-y^2/(2a_S^2)} \frac{\pi w}{1 - e^{-\pi w}} \times \\ &\int_0^\infty dz z e^{-z^2/(2a_S^2)} I_0(yz/a_S^2) \left| {}_1F_1\left(\frac{iw}{2}, 1; \frac{iwz^2}{2}\right) \right|^2 \end{aligned} \quad (3)$$

is a magnification factor that accounts for effects of both the finiteness of the source and wave optics, with ${}_1F_1$ the confluent hypergeometric function of the first kind. (We use the Python package `mpmath` [17] to evaluate

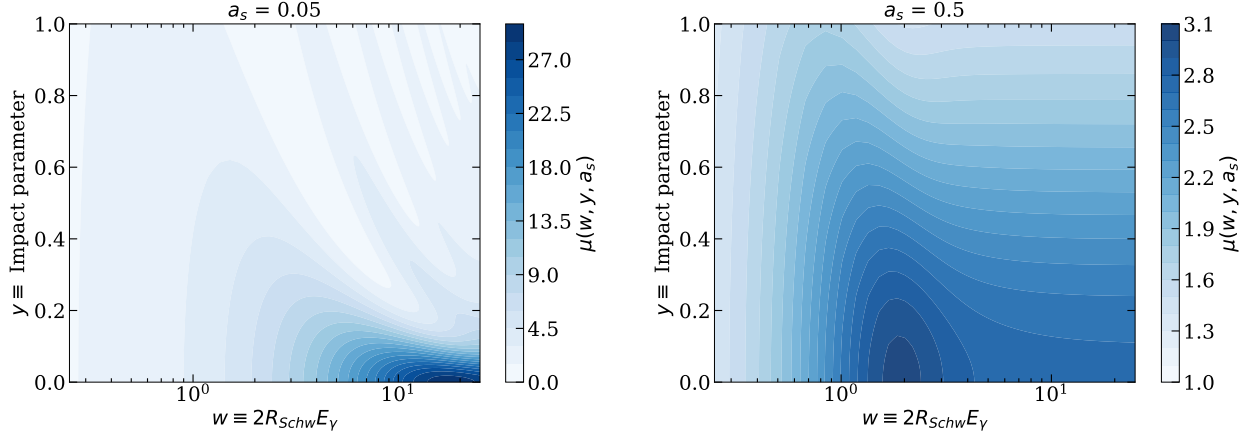


FIG. 2. Contours of the magnification factor in Eq. (3) for point-like lenses in the plane of the wave/geometric optics demarcation parameter w (Eq. (4)) and the impact parameter y , for the source sizes a_s as indicated. See Sec. II for a discussion of the features here.

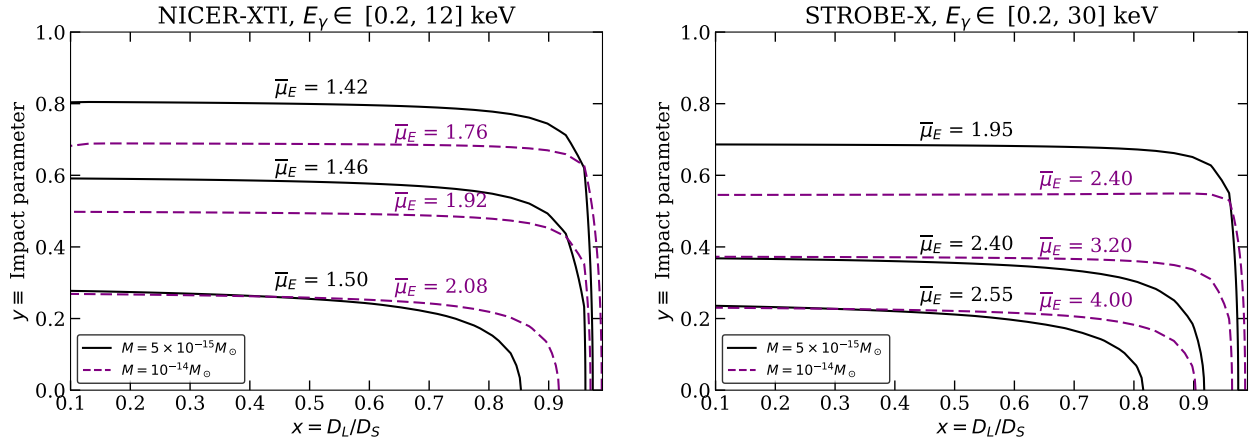


FIG. 3. Contours of the source-specific energy-averaged magnification factor in Eq. (2) for the x-ray pulsar SMC X-1 (source size: 20 km, distance from Earth: 64 kpc) at NICER and STROBE-X, with their detection energy ranges as indicated. See Sec. II for a discussion of the features here.

${}_1F_1$.) The intensity of the source is here assumed to follow a Gaussian profile $\propto \exp(-|\vec{y} - \vec{z}|^2/2a_s^2)$, and $I_0(z) = (1/2\pi) \int_0^{2\pi} e^{z \cos \theta} d\theta$ is the zeroth-order modified Bessel function of the first kind [18].

The effect of wave optics is encapsulated by the parameter

$$w \equiv \frac{4GME_\gamma}{\hbar c^3} = \frac{2R_{\text{Schw}}E_\gamma}{\hbar c} \quad (4)$$

$$\Rightarrow E_\gamma = 33.5 \text{ keV} \left(\frac{10^{-15} M_\odot}{M} \right) w,$$

where $R_{\text{Schw}} = 2GM/c^2$ is the Schwarzschild radius of the PBH and E_γ is the photon energy. In the limit of $w \gg y^{-1}$ (where the impact parameter y is typically $\mathcal{O}(1)$) the extent of the lens well exceeds the photon wavelength, and Eq. (3) reduces to the expression ob-

tained from geometric optics [18–21] as seen by inspecting the behavior of ${}_1F_1$. In the limit of $w \lesssim y^{-1}$ wave optics effects become important, and the magnification tends to be suppressed for $w \ll y^{-1}$. Thus Eq. (4) also roughly marks the smallest PBH mass that can be probed by an instrument, corresponding to the largest energy it can detect, beyond which wave effects degrade the sensitivity. Thus for {NICER, STROBE-X/LOFT-P, RXTE}, which reach energies of {12, 30, 60} keV, the wave effects tend to suppress microlensing signals for $M < \{28, 11, 5.6\} \times 10^{-16} M_\odot$. Our proposed detector X μ would reach 1000 keV, hence PBH masses down to $3.4 \times 10^{-17} M_\odot$. The exact value of M down to which a given instrument can reach is determined by a few other factors, which will be discussed soon.

We depict the effects of finite source and wave optics

in Figure 2 with contours of the magnification factor in Eq. (3) in the space of w and lens impact parameter y , for source sizes a_S of 0.05 and 0.5. Scanning from left to right in both panels, we see that μ is suppressed for $w \ll 1$, deep in the wave optics regime, peaks at some intermediary w , and stabilizes at some $w \gg 1$ deep in the geometric optics regime. Smaller impact parameters y generally tend to produce larger magnifications, as expected. Comparing across panels, the $a_S = 0.5$ case typ-

ically produces smaller magnifications as expected: the more extended a source is on the lens plane, the less it is focused by the lens and hence the weaker the magnification [4, 22]. For $a_S = 0.05$ large fluctuations in μ are visible in the region of transition between wave and geometric optics, $w = \mathcal{O}(1 - 10)$, a reflection of the rapid oscillation of the hypergeometric function in this region, best seen by taking appropriate limits of the a_S -independent, w -dependent piece of the integrand in Eq. (3) [19]:

$$\frac{\pi w}{1 - e^{-\pi w}} \left| {}_1F_1\left(\frac{iw}{2}, 1; \frac{iwz^2}{2}\right) \right|^2 = \begin{cases} 1 + \frac{\pi w}{2} + \frac{w^2}{2}(\pi^2 - 3z^2) & , w \ll 1, \\ \frac{1}{z\sqrt{4+z^2}} \left[2 + z^2 + 2 \sin \left[w \left(\frac{1}{2} z \sqrt{4+z^2} + \log \left| \frac{\sqrt{4+z^2}+z}{\sqrt{4+z^2}-z} \right| \right) \right] \right] & , w \gtrsim z^{-1}. \end{cases} \quad (5)$$

The white bands where $\mu \rightarrow 0$ depict regions where there is complete destructive interference. For $a_S = 0.5$, however, these oscillations are not visible since they are averaged out quickly via the tempering effect of the finite source, captured in Eq. (3) by the modified Bessel function term in the integrand; see the detailed illustrations in Ref. [19].

In Figure 3 we show contours of the energy-averaged detector- and source-specific magnification in Eq. (2) in the plane of the impact parameter y and fractional distance to the lens x . The source here is taken to be the x-ray pulsar SMC X-1 in the Small Magellanic Cloud at a distance $d = 64$ kpc, with the source size, i.e., the radius of the emission region, taken to be $R_S = 20$ km as done in Ref. [3]. The SED of this pulsar is taken as [23]

$$\mathcal{F}(E_\gamma) = \begin{cases} (E_\gamma/\text{keV})^{-0.93} & , E_\gamma \leq 6 \text{ keV}, \\ (E_\gamma/\text{keV})^{-0.93} e^{-(E_\gamma - 6 \text{ keV})/7.9 \text{ keV}} & , E_\gamma > 6 \text{ keV}. \end{cases} \quad (6)$$

The left and right panels depict respectively the currently operational X-ray Timing Instrument (XTI) on NICER and the forthcoming STROBE-X satellite, spanning energy ranges of [0.2, 12] keV and [0.2, 30] keV, whose effective areas $\mathcal{A}(E)$ are given in Ref. [14]. We display two sets of contours corresponding to PBH masses $5 \times 10^{-15} M_\odot$ and $10^{-14} M_\odot$, having Schwarzschild radii of $(13.4 \text{ keV})^{-1} \equiv 1.5 \times 10^{-2} \text{ nm}$ and $(6.7 \text{ keV})^{-1} \equiv 2.9 \times 10^{-2} \text{ nm}$ respectively.

For a given y the values of $\bar{\mu}_E$ obtained at STROBE-X are seen to be generically larger than at NICER. This is because STROBE-X can reach higher photon energies than NICER, so that it samples more of the geometric optics-dominated (as opposed to wave optics-dominated) region of microlensing, leading to overall stronger magnification. In both panels the heavier PBH obtains higher magnification for comparable (x, y) values, as once again it lies more in the geometric optics region, i.e., w is larger

for a given photon energy. As expected, the magnification increases as y is reduced. An interesting effect is the rate of variation of $\bar{\mu}_E$ across y , which is faster (slower) for the heavier (lighter) PBH. This is once again due to the wave vs geometric optics at play. As seen from Fig. 2, the magnification varies slowly with y in the wave optics ($w \ll y^{-1}$) region and more quickly in the geometric optics ($w \gg y^{-1}$) region. The contours in Fig. 3 rapidly go to $y = 0$ beyond some value of $x = x_{\text{max}}$. This is the result of the finite source effect, which suppresses the magnification for lenses too close to the source. If larger $\bar{\mu}_E$ values are desired, it comes with the price of smaller x_{max} in order to obtain a small source size on the lens plane.

II.2. Identifying microlensing in x-ray pulsar data

Having reviewed microlensing in the x-ray regime, we now turn to how microlensing events may be identified in data. We will make use of information on both count rates and energies of the photons detected at x-ray telescopes.

To uncover a PBH transit producing excess photon counts such as in microlensing, we follow the statistical prescription in Ref. [3]. Assuming that time-binned photon counts are independent events and follow a Gaussian distribution, we demand that there are N_{consec} bins with photon counts that are at least N_σ standard deviations (σ_B) greater than the mean counts per second B . The values of N_{consec} and N_σ must be chosen prudently so that the signal is statistically significant, i.e., the probability that such bins are produced by the statistical fluctuations must be sufficiently minuscule. We will soon show that $N_{\text{consec}} = 3$ and $N_\sigma = 3$ are optimal choices, which we will use for the rest of this work.

We must also ensure that a magnified signal (as defined below) has not simply arisen from a large number of statistical samples, i.e., from the look-elsewhere effect.

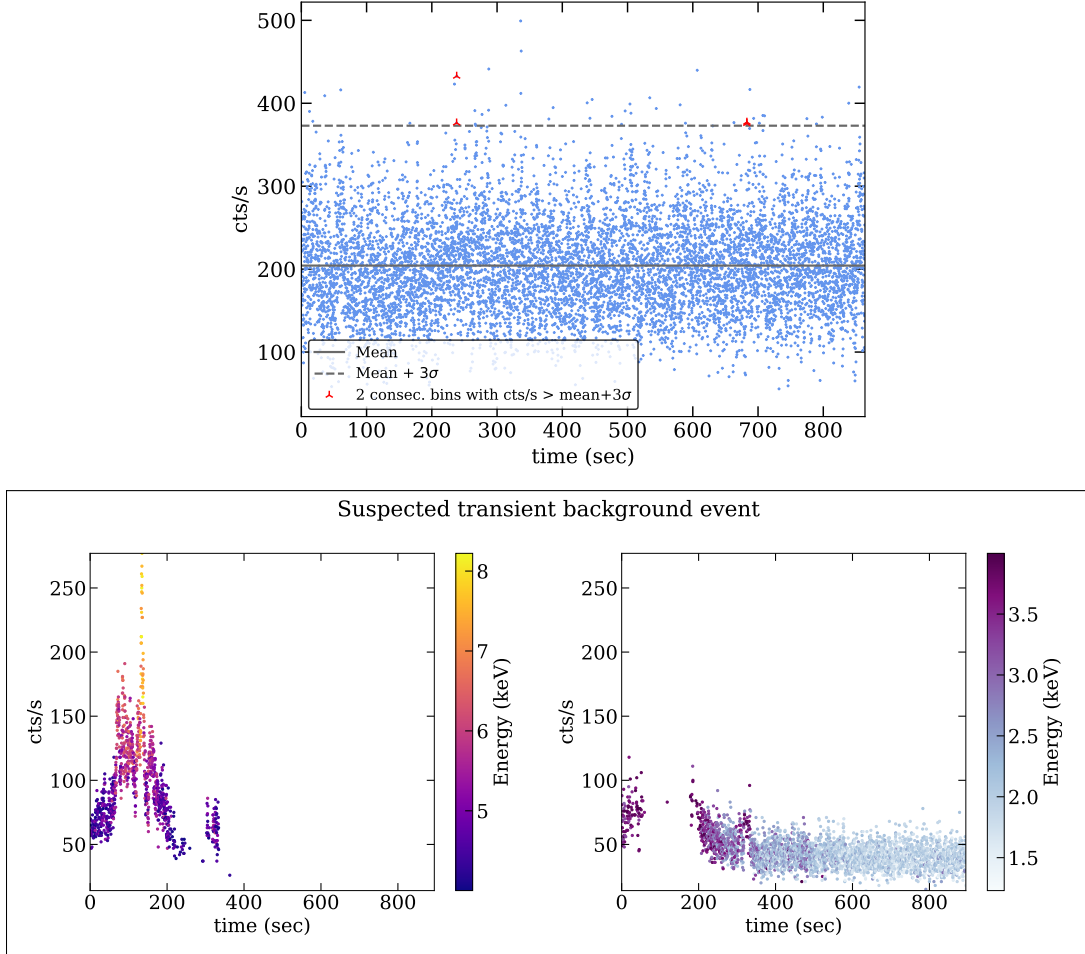


FIG. 4. **Top:** An 864-second segment (observation ID = 6535010301) of the x-ray pulsar SMC-X1 at NICER-XTI, binned by 0.1 seconds. With horizontal lines are shown the mean B and the count rate 3 standard deviations σ_B from it, and with red crosses are shown regions with 2 consecutive bins with count rate greater than $B + 3\sigma_B$. **Bottom:** Another segment (observation ID = 6535010801) showing a transient event. To confirm this as an occurrence unrelated to microlensing, such as an x-ray flare or interaction of atmospheric electrons with the detector, we inspect the event in two windows of energy (here with 0.2 second time-binning). Microlensing induced by PBHs in the geometric optics regime would be achromatic and thus appear the same in the two windows. See Sec. II.2 for further details.

The probability of obtaining 3 consecutive events above the 3σ threshold should be smaller than

$$\frac{t_{\text{bin}}}{t_{\text{exp}}} = 1.9 \times 10^{-8} \left(\frac{t_{\text{bin}}}{0.1 \text{ s}} \right) \left(\frac{60 \text{ days}}{t_{\text{exp}}} \right), \quad (7)$$

where t_{exp} is the exposure time. This probability \mathbb{P} indeed satisfies the above condition for the 60-day exposures we consider, as it is $\mathbb{P}(N_\sigma) = (1 - \Phi(N_\sigma))^{N_{\text{consec}}} = 2.5 \times 10^{-9}$, where $\Phi(x) = \frac{1}{2} \left(1 + \text{erf}(x/\sqrt{2}) \right)$ is the Gaussian cumulative distribution function (CDF) [3].

The minimum energy-averaged magnification required to detect microlensing events at a given telescope, for count rates that are $n_\sigma \sigma_B$ away from the mean, is given as

$$\bar{\mu}_{\text{thresh}} = \frac{1 + N_\sigma \sigma_B / B}{1 + n_\sigma \sigma_B / B}. \quad (8)$$

As we will see in Sec. III, a conservative and reasonable choice of n_σ is -1, which we will adopt. Variations in binning time $t_{\text{bin}} \rightarrow \tilde{t}_{\text{bin}}$ and bin counts $B \rightarrow \tilde{B}$ can be incorporated in Eq. (8) by the replacement $\sigma_B/B \rightarrow (\sigma_B/B)/\sqrt{(\tilde{B}/B)(\tilde{t}_{\text{bin}}/t_{\text{bin}})}$.

To justify our choices of N_{consec} , N_σ and n_σ visually, we show in Figure 4 an 864-second sample, with $t_{\text{bin}} = 0.1$ sec, of the NICER-XTI data on SMC-X1 extracted using HEASoft v6.33.2 [24] with `nicer12` and `nicer13-1c` pipelines. In this sample the mean $B = 204.26$ cts/s, which is indicated with a solid horizontal line, and the standard deviation $\sigma_B = 56.23$ cts/s; the $3\sigma_B$ deviation from the mean is indicated with a dashed horizontal line. Note that $\sqrt{B t_{\text{bin}}} = 4.52$ is only slightly smaller than $\sigma_B t_{\text{bin}}$, implying that the assumption of Gaussian statistics is good and that intrinsic variability in the count

rate is small. The threshold magnification in Eq. (8) is then $\bar{\mu}_{\text{thresh}} = 2.5$. We mark with red crosses bins that show 2 consecutive counts that are more than $3\sigma_B$ from the mean. We find no regions with 3 consecutive bins satisfying the criterion.

The count rate, and hence the threshold magnification in Eq. (8), is determined by the source SED as well as the effective area of the detector. For our proposed telescope $X\mu$, we assume an energy-dependent effective area that is a combination of three parts: [i] for $E \in [0.2, 50]$ keV we adopt the $\mathcal{A}(E)$ of the Large Area Detector (LAD), to be used on STROBE-X [13] and eXTP [25]; [ii] for $E \in [50, 260]$ keV we take the $\mathcal{A}(E)$ profile of the cadmium zinc telluride “medium energy” detector proposed to be used in Daksha [15], and scale the normalization up by a factor of 2, [iii] for $E \in [260, 980]$ keV we take the $\mathcal{A}(E)$ profile of the NaI “high energy” detector of Daksha and again rescale by a factor of 2. The energy-averaged detector area weighted by the source SED, $\bar{\mathcal{A}} = \int_{E_{\text{min}}}^{E_{\text{max}}} dE \mathcal{F}(E) \mathcal{A}(E) / \int_{E_{\text{min}}}^{E_{\text{max}}} dE \mathcal{F}(E)$, is 30.9 and 46.8 times bigger for STROBE-X and $X\mu$ respectively as compared to NICER. Rescaling $\bar{\mu}_{\text{thresh}}$ suitably by $\sqrt{\bar{\mathcal{A}}}$ we obtain $\bar{\mu}_{\text{thresh}} = 1.21$ for STROBE-X and $\bar{\mu}_{\text{thresh}} = 1.17$ for $X\mu$, which we use for obtaining projections in Sec. III.

In selecting observation samples for analysis, care must be taken to remove bins that are contaminated by x-ray flares and bursts, as well as atmospheric backgrounds such as trapped electrons (TREL), precipitating electrons (PREL), and low-energy electrons (LEEL) [26]. This may be done manually by visual inspection for distinct rise-and-falls in photon counts, but to ascertain that we are not discarding microlensing events, we also perform the following procedure. Microlensing in the geometric optics regime (i.e., for PBHs larger than the photonic wavelength) is achromatic: it produces source frequency-independent magnification. We exploit this fact to look for similarities in the light curve in two different energy windows for suspected flares or PREL events. The bottom panel of Figure 4 shows an example of a suspected x-ray flare in the SMC-X1 NICER data, with either panel displaying photon counts with energies $>$ and ≤ 4 keV. (To obtain this plot we use information on individual photon energies and detection timestamps, and then show the count rate in 0.2 sec bins.) If this had been a microlensing event, these panels would have looked alike, but they look extremely dissimilar. That the higher-energy counts alone occur as an excess confirms that this event is indeed an x-ray flare or burst.

A diagnostic like this serves not only to distinguish microlensing events from background transients, but to also roughly inform us of the mass of the PBH should a true microlensing event be observed. If the count rate vs time of a suspected signal event corresponds to the characteristic shape of the light curve expected from microlensing, and is seen to be identical – or more practically, statistically consistent – in two or more energy windows, then we may be sure that the transiting PBH is massive enough

to be in the geometric optics regime, where microlensing is indeed achromatic. The geometric vs wave optics nature of microlensing may be further verified by extracting the lens mass, at least broadly, by:

[i] comparing the event time scale with the lens transit time, roughly $2r_E$ divided by the transverse speed of dark matter. Equation (1) gives r_E in terms of M and x , if the dark matter speed is taken as its typical value (about 200 km/s);

[ii] fitting the light curve to obtain the magnification, which contains further information about M and x via Eq. (2).

The range of x can be further narrowed to some $\mathcal{O}(0.1)$ value by considering its probability distribution, which is the differential optical depth $\pi r_E^2(x) n_{\text{PBH}}(x) dx$, where n_{PBH} is the PBH number density along the line of sight to the source.

If the PBH mass is in the wave optics regime, confirmation of microlensing would be unfortunately more complicated. This is because in this regime the microlensing magnification is frequency-dependent, as discussed in Sec. II.1 and in, e.g., Refs. [18–20]. An additional complication is that magnifications are suppressed for impact parameters $y > w^{-1}$, as seen in Sec. II.1. Also, the signal would be initially and finally achromatic during the transit but chromatic when the lens is nearest to the source on the lens plane. This may be seen from Eq. (5), where the sine term $\rightarrow 0$ for fast oscillations. In this regime the detector energy resolution becomes important: if it is smaller than the change in w over which the magnification varies appreciably for a suspected lens mass, chromatic microlensing may be measured. Perhaps astrometric microlensing may lift the degeneracies discussed here, as demonstrated for microlensing in optical frequencies [27], but this could be challenging for x-ray microlensing due to uncertainties in pulsar emission and localization. We leave the question of diagnosing microlensing signatures in the wave optics regime to future investigation.

III. EVENT RATES AND TELESCOPE SENSITIVITIES

Assuming that the PBH mass spectrum is monochromatic (i.e., that all PBHs have a single mass), and that their velocities follow a Maxwell-Boltzmann distribution, the differential rate of microlensing with respect to event timescale t_E per source pulsar is given by [33]

$$\frac{d\Gamma}{dt_E} = f_{\text{PBH}} \frac{2D_S}{M v_0^2} \int_0^1 dx \rho_{\text{DM}}(x) v_E^4(x) e^{-v_E^2/v_0^2} \times \int_0^{y_T(x)} \frac{dy}{\sqrt{y_T^2 - y^2}} \times \mathbb{P}(n_\sigma), \quad (9)$$

where $v_E \equiv 2r_E \sqrt{y_T^2 - y^2} / t_E$, with $y_T(x)$ the maximum impact parameter within which the magnification $\geq \bar{\mu}_{\text{thresh}}$ as illustrated in Fig. 3, v_0 is the halo circular

| x-ray pulsar | net exposure (days) | D_S (kpc) | (ℓ, b) | σ_B/B |
|--------------|---------------------|-------------|--------------------------------|--------------|
| SMC X-1 | 1.74 | 64 [28] | $(300.41^\circ, -43.56^\circ)$ | 0.28 |
| Cyg X-2 | 5.47 | 11 [29] | $(87.33^\circ, -11.32^\circ)$ | 0.02 |
| Vela X-1 | 4.46 | 2 [30] | $(263.06^\circ, 3.93^\circ)$ | 0.25 |
| Crab pulsar | 4.76 | 2 [31] | $(184.56^\circ, -5.78^\circ)$ | 0.01 |

TABLE I. X-ray pulsars in the NICER dataset [32] with significant count rates and small intrinsic variability σ_B/B , and the net telescope exposure on them. Also given are their distances from Earth and location in Galactic co-ordinates. Due to its distance SMC X-1 provides the greatest microlensing optical depth, thereby dominating the total event rate. See Sec. III for further details.

velocity $\simeq 240$ km/s, f_{PBH} is the mass fraction of PBHs making up the dark matter density ρ_{DM} , and $\mathbb{P}(n_\sigma)$ is the fraction of bins in the dataset with count rate higher than $B + n_\sigma \sigma_B$ for 3 consecutive bins. We find that $\mathbb{P}(-1) = 0.596$ for a Gaussian CDF with $n_\sigma = -1$. (For $n_\sigma = -2$ we have $\mathbb{P}(-2) = 0.93$, which would be an aggressive choice, and for $n_\sigma = 0$ our event acceptance would be low with $\mathbb{P}(0) = 0.13$.) Note that in general the first integral in Eq. (9) evaluates to non-zero values only up to some $x = x_{\text{max}}$ since, as seen from Fig. 3, $y_T(x) \rightarrow 0$ above x_{max} , thereby making the second integral vanish.

We show results for two different spatial distributions of ρ_{DM} , ignoring the line-of-sight DM density in satellite galaxies (where some of our pulsars are situated) as it contributes only about 10% to the event rate. First we take the Einasto profile,

$$\rho_{\text{Ein}}(r) = \frac{M_0}{4\pi r_s^3} e^{-(r/r_s)^\alpha}, \quad (10)$$

$$r = \sqrt{r_\odot^2 + x^2 D_S^2 - 2r_\odot x D_S \cos \ell \cos b},$$

where $r_\odot = 8.33$ kpc is the distance of the Sun from the Galactic Center, and (ℓ, b) are the Galactic co-ordinates of the source. Recent studies [34] using photometry data from Gaia DR3, 2MASS and WISE combined with SDSS-APOGEE DR17 spectra show that Milky Way circular velocities for galactic radii ≤ 30 kpc are best fit by the above Einasto profile with a normalization mass $M_0 = 6.2 \times 10^{10} M_\odot$, scale radius $r_s = 3.86$ kpc, and slope parameter $\alpha = 0.91$, which we adopt. As a cored Einasto profile is found to better fit the circular velocities estimated in Ref. [34] than, say, a cuspy Navarro-Frenk-White (NFW) profile, the virial mass of the Milky Way turns out to be smaller than previous estimates, which is consistent with the findings of Refs. [35, 36] that use Gaia DR3 data at smaller galactic radii. The upshot is that the use of Eq. (10) makes dark matter densities, hence the microlensing optical depth, generally smaller than in earlier works such as Refs. [4, 8, 11].

Nevertheless, we also derive optimistic projections by assuming the NFW profile,

$$\rho_{\text{NFW}}(r) = \frac{\rho_0}{(r/r_s)(1 + r/r_s)^2}, \quad (11)$$

to make direct comparisons with earlier literature and which may better describe the Galactic halo in future

and/or complementary data. To fix the unknown parameters in Eq. (11), we [i] fix $\rho_\odot = 0.44$ GeV/cm³ as the dark matter density at the solar position as obtained from the best-fit of Eq. (10); this ensures that dark matter densities at least near the Earth are comparable in the two profiles we consider, [ii] take the mass of dark matter within $r = 60$ kpc as $4.7 \times 10^{11} M_\odot$ as estimated by the SDSS survey in Ref. [37]. These give $\rho_0 = 0.95$ GeV/cm³ and $r_s = 11.46$ kpc. Other choices that fix NFW parameters, as well as the best-fit generalized-NFW profile in Ref. [34], yield constraints that are quite similar to those obtained with the best-fit Einasto profile.

The total number of microlensing events expected in a telescope, summing over pulsar targets labelled by i with individual observation times T_{obs}^i , is now

$$N_{\text{ev}} = \sum_i T_{\text{obs}}^i \int_{t_{\text{min},i}}^{t_{\text{max},i}} dt_E \frac{d\Gamma_i}{dt_E}, \quad (12)$$

where $t_{\text{min},i}$ is the binning time ($= 0.1$ sec here) and $t_{\text{max},i}$ is the net exposure for the source i . These integration limits are chosen as the shortest and longest timescales over which a microlensing event can be observed at a telescope. Thus constraints on the unknowns f_{PBH} and M may be derived by comparing N_{ev} with the observed number of events under the no-PBH null hypothesis. For example, if zero events are observed, using Poisson statistics the 90% C.L. limit can be obtained by setting $N_{\text{ev}} = 2.3$. In practice, we evaluate the integral in Eq (12) using the analytic form identified in the appendix of Ref. [8].

III.1. Prescription for obtaining microlensing limits

Before we discuss our main results, let us first summarize the series of steps for obtaining the constraints as described in the text up to this point.

(1) Select x-ray pulsar sources with high count rates, low intrinsic variability, and possibly large distances to maximize the PBH microlensing optical depth.

(2) Obtain data on count rate vs time and photon energies on the x-ray pulsar sources, combining segments such as those in Fig. 4. Use appropriate data-processing pipelines.

(3) Inspect the dataset for transient excesses. To verify them as non-microlensing events, check the count rate in

two or more different photon energy windows such as in the bottom panel of Fig. 4.

(4) If the count rates in different energy windows are dissimilar, discard the corresponding time bins. If they are similar, investigate further if the shape of the light curve corresponds to a microlensing signature. Attempt to break degeneracies in microlensing free parameters as discussed at the end of Sec. II.2.

(5) From the subset of data with chromatic excesses removed, obtain the mean and standard deviation of the count rate. Optimize choices of N_{consec} , N_{σ} and n_{σ} . Then estimate the threshold magnification $\bar{\mu}_{\text{thresh}}$ from Eq. (8).

(6) Use this $\bar{\mu}_{\text{thresh}}$, the effective area $\mathcal{A}(E)$ and the source SED $\mathcal{F}(E)$ to obtain y_T vs x from Eq. (2) as in Fig. 3.

(7) Finally, use the microlensing event rate in Eq. (9) to estimate the total number of events expected (Eq. (12)). Use appropriate statistics to report limits at the desired confidence level.

III.2. Results

In Fig. 1 we display with dashed (dotted) curves the NFW (Einasto) profile 90% C.L. limits obtained with current data at NICER, with effective area $\mathcal{O}(10^{-2} - 10^{-1})$ m², on the pulsars listed in Table I, after removing transient excesses caused by flares, electron backgrounds, etc. These pulsars were selected for the appreciable photon count rates they yielded at NICER, bright as they are. Despite a somewhat lower exposure compared to Cyg X-2, Vela X-1 and the Crab pulsar, the SMC X-1 pulsar dominates the net microlensing event count in Eq. (12) due to its large distance from Earth that results in a relatively high microlensing optical depth. From SMC X-1 count rate data such as the sample in Fig. 4, using Eq. (8) we get the threshold energy-averaged magnification $\bar{\mu}_{\text{thresh}} = 2.5$. We see that the data accumulated so far at NICER could only set $f_{\text{PBH}} < 20$ in the mass range of about $10^{-14} - 10^{-13} M_{\odot}$. If the exposure on SMC X-1 were increased to 60 days, we see that NICER can reach $f_{\text{PBH}} = 0.7$ for $M = 2 \times 10^{-14} M_{\odot}$ and can generally probe the mass range $(1 - 5) \times 10^{-14} M_{\odot}$ for $f_{\text{PBH}} \leq 1$. Such an exposure is justified by the enormous significance of the physics case here. We also believe it is entirely feasible as this exposure is much less than that obtained at NICER for some sources, e.g., 9–12 months [38], and comparable to that of other sources, e.g., PSR B1937+21, as seen in the NICER data archive [32].

We also show the 30-day reaches of future x-ray telescopes with effective areas about an order of magnitude greater than that of NICER. For STROBE-X we use SMC X-1 as the source. For $X\mu$ we assume a hard x-ray pulsar source that is at $D_S = 64$ kpc, with intrinsic variability σ_B/B that of SMC X-1 (as in Table I), and an energy spectrum that is the same as the Crab pulsar [39], which provides a flux orders of magnitude higher than

that of SMC X-1 for 10 – 1000 keV energies. By placing this source far away our count rate is $1/D_S^2$ -suppressed, but we gain in microlensing optical depth. As mentioned below Eq. (6), these telescopes can also probe photon energies higher than at NICER. We see in Fig. 1 that $X\mu$ could probe much smaller PBH masses than NICER, down to $2.5 \times 10^{-17} M_{\odot}$, while STROBE-X can reach down to about $10^{-15} M_{\odot}$. This is because these telescopes, by virtue of detecting smaller x-ray wavelengths than NICER, can overcome the wave optics effect and observe microlensing by smaller/lighter PBHs. Note that requiring an excess over 3 consecutive 0.1 sec bins (as below Eq. (8)) implies requiring a transit time across r_E of 0.3 sec, which is expected on average for $M > 10^{-15} M_{\odot}$, whereas the $X\mu$ limits go to smaller lens masses. This is possible by shrinking t_{bin} suitably which does not unduly affect the counts per bin due to the large collecting power of the telescope, nor the threshold magnification as per the discussion under Eq. (8). As such, the microlensing event count may slightly increase if t_{min} in Eq. (12) is set to the new t_{bin} , but our $X\mu$ estimate uses $t_{\text{min}} = 0.1$ sec and must be taken as a conservative projection.

STROBE-X and $X\mu$ also reach smaller f_{PBH} of $\mathcal{O}(0.1)$ than NICER with less run-time. This is due to their larger effective areas that result in smaller threshold magnification, in turn giving greater event rates as per Eq. (9). We see that the limits on f_{PBH} appear to be proportional to \sqrt{M} for large PBH masses. This may be broadly understood as follows. The PBH velocities are roughly constant, so that the only M -dependence in Eq. (9) is in the term outside the integrals. Since $t_E \propto \sqrt{M}$, Eq. (12) implies that $f_{\text{PBH}} \propto \sqrt{M}$ for a fixed N_{ev} . Our results may be compared with that of Ref. [3], which shows that with 300 days of exposure the future eXTP satellite would reach down to $f_{\text{PBH}} \simeq 0.1$, and Athena, Lynx and AstroSat to $f_{\text{PBH}} \simeq 0.3$. Shorter exposures such as we have used will weaken the sensitivities of Ref. [3] proportionally.

IV. DISCUSSION AND SCOPE

In this work we have investigated the sensitivity of x-ray telescopes studying x-ray pulsars to microlensing by sub-atomic size primordial black holes. Our results are summarized in Figure 1. We have also described a spectral diagnostic to confirm a microlensing signal in the geometric optics regime, which can further be confirmed by measuring the timescale and magnification of events. We re-emphasize that, while searches at the ongoing NICER and planned STROBE-X telescopes would be definitely exciting, commissioning a new, large, broadband x-ray satellite dedicated to gravitational microlensing surveys would be even more worthwhile in light of the wealth of fundamental physics to be mined.

X-ray microlensing in these telescopes would help to uncover not only point-like lenses such as PBHs, but also, as mentioned in the Introduction, dark matter in struc-

tures with extent comparable to the (point-like) Einstein radius, which would produce non-trivial magnification curves. It may even be possible to distinguish between the possibilities, such as microhalos of various density distributions, boson stars, etc., via machine learning techniques [40]. Whatever be the type of lens, mass functions other than the simple monochromatic one assumed here may be used to set limits, such as done in Ref. [41].

Our work is the first to point out that the PBH evaporation limit at around $10^{-16} M_\odot$, the lower end of the PBH mass window, may be probed with a minimal microlensing setup involving hard x-ray pulsars; see Appendix B for more sophisticated setups. But the PBH mass window itself may be wider than previously supposed. If black hole evaporation, which has never been observed, proceeds at a rate slower than Hawking's prediction as may happen via the memory burden effect [42], then the extant limits on PBH masses from evaporation (at $M \gtrsim 10^{-16} M_\odot$) may be greatly weakened [43]. It is even possible that PBHs as light as $10^{-28} - 10^{-23} M_\odot$ are allowed to comprise all the dark matter [44]. To catch very light PBHs in microlensing would require sources emitting photons with wavelengths even smaller than x-rays. Perhaps gamma-ray pulsars shining copiously to give sufficient statistics at such detectors as Fermi-LAT [45] may be valuable. Even in the absence of evaporation-slowing effects, PBH microlensing campaigns involving hard x-ray sources and gamma-ray pulsars would be worthwhile: they automatically constrain non-PBH compact dark matter structures that are smaller than the relevant Einstein radii. In this light our $X\mu$ reach in Fig. 1 at low M must be read by ignoring the evaporation constraints.

All told, the time has come to coax dark matter out of one of its famed hideouts.

ACKNOWLEDGMENTS

We are indebted to Paul Ray for key insights on the operation of NICER and Abhisek Tamang for help with HeaSOFIT. We further thank Varun Bhalariao, Priyanka Gawade, Ranjan Laha, Surhud More, Suvodip Mukherjee, Avinash Kumar Paladi, Akash Kumar Saha, Vibhor Kumar Singh, Abhishek Tiwari, Ujjwal Kumar Upadhyay, Himanshu Verma, and Anna Watts for helpful discussion.

Appendix A: Background material on microlensing

In this appendix we provide derivations for some formulae in Sec. II. For detailed treatments of microlensing we refer the reader to Refs. [16, 19].

We start with some generic notions. Consider the background metric $g_{\mu\nu}$ with a gravitational potential U due to a point-like lens, given by

$$ds^2 \equiv g_{\mu\nu} dx^\mu dx^\nu = -(1+2U)dt^2 + (1-2U)d\vec{r}^2. \quad (\text{A1})$$

As shown in Ref. [46], for $U \ll 1$ we can treat the propagating degree of freedom of an electromagnetic wave as a massless scalar field ϕ obeying

$$\partial_\mu(\sqrt{-g} g^{\mu\nu} \partial_\nu \phi) = 0. \quad (\text{A2})$$

Setting $\phi(\vec{r}, t) = \Phi(\vec{r})e^{-i\omega t}$, we get

$$(\nabla^2 + \omega^2)\Phi(\vec{r}) = 4\omega^2 U\Phi(\vec{r}). \quad (\text{A3})$$

We can now define an amplification factor in the frequency domain, F , as the ratio of the solutions to Eq. (A3) for non-zero and zero U , with the magnification given by

$$\mu(\omega, \vec{y}) = |F(\omega, \vec{y})|^2 \quad (\text{A4})$$

for a source angular position \vec{y} as defined below Eq. (1). Switching variables to w as defined in Eq. (4), we have [18]

$$F(w, \vec{y}) = \frac{w}{2\pi i} \int d^2\vec{\rho} e^{i\omega T(\vec{\rho}, \vec{y})}, \quad (\text{A5})$$

where $T(\vec{\rho}, \vec{y})$ is the time delay function

$$T(\vec{\rho}, \vec{y}) = \frac{1}{2}|\vec{\rho} - \vec{y}|^2 - \psi(\vec{\rho}) \quad (\text{A6})$$

for a dimensionless lensing potential $\psi(\vec{\rho})$. For a spherically symmetric lens, $\psi(\vec{\rho})$ only depends on $\rho \equiv |\vec{\rho}|$. Taking θ as the angle between $\vec{\rho}$ and \vec{y} , we now have

$$F(w, y) = -i\omega e^{i\omega y^2/2} \int_0^\infty d\rho J_0(w\rho y) x e^{i\omega(\frac{1}{2}\rho^2 - \psi(\rho))}, \quad (\text{A7})$$

where

$$J_0(z) = \frac{1}{\pi} \int_0^\pi d\theta e^{iz \cos \theta} \quad (\text{A8})$$

is the Bessel function of the first kind of zeroth order.

The lensing potential $\psi(\rho)$ is obtained by solving the convergence equation [16]

$$\vec{\nabla}_\rho^2 \psi = 2 \frac{\Sigma(\vec{\rho})}{\Sigma_{\text{crit}}}, \quad (\text{A9})$$

where Σ is a surface density obtained by projecting the lens' density onto the lens plane and $\Sigma_{\text{crit}} \equiv c^2 D_S / (4\pi G D_L D_{LS})$ is a critical mass density.

Point-like lenses. For lenses with extent $\ll r_E$ such as PBHs, $\psi(x) = \log x$, so that from Eqs. (A4) and (A7) and a bit of algebra, we have

$$\mu(w, y) = \frac{\pi w}{1 - e^{-\pi w}} \left| {}_1F_1\left(\frac{iw}{2}, 1; \frac{iwy^2}{2}\right) \right|^2, \quad (\text{A10})$$

where we have used the relations

$$\int_0^\infty x^m e^{-\alpha x^2} J_n(\beta x) dx = \frac{\beta^n \Gamma(\frac{m+n+1}{2})}{2^{n+1} \alpha^{\frac{m+n+1}{2}} \Gamma(n+1)} \times {}_1F_1\left(\frac{m+n+1}{2}, n+1; -\frac{\beta^2}{4\alpha}\right),$$

and

$$\Gamma(1 + iy)\Gamma(1 - iy) = \frac{\pi y}{\sinh(\pi y)}.$$

In the limit $y \rightarrow 0$, ${}_1F_1 \rightarrow 1$ and we get the maximum magnification during transit as

$$\mu_{\max} = \frac{\pi w}{1 - e^{-\pi w}}.$$

The effect of finite source size. To account for the finite extent of the source, consider a Gaussian distribution of source intensity,

$$W(\vec{y}, \vec{r}) = \exp\left(-\frac{|\vec{y} - \vec{r}|^2}{2a_s^2}\right). \quad (\text{A11})$$

Then the intensity-averaged magnification

$$\mu(w, y, a_s) = \frac{\int d^2r W(y, r) \mu(w, r)}{\int d^2r W(y, r)} \quad (\text{A12})$$

gives Eq. (3) under the assumption of circular symmetry, i.e., that W depends only on $r \equiv |\vec{r}|$

Appendix B: Other probes of the PBH mass window

We enumerate here alternative proposals in the literature to close the PBH mass window.

[i] Interference fringes of the two microlensing images showing up as modulations in the energy spectrum, a.k.a. “femtolensing”, with about 100 or more gamma ray burst

(GRB) sources in order to overcome the finite source effect [47].

[ii] Differences in magnification as seen simultaneously by two observing instruments separated by a finite distance, a.k.a. “parallax microlensing” [48]. With more than 1000 GRBs, the future *Daksha* system can probe the PBH mass window with one satellite each orbiting the Earth and the Moon [49].

[iii] Transits of light PBHs through the Solar System, estimated to occur about once in a decade, may affect precision ephemerides [50].

[iv] Stellar capture of PBHs in dark matter-rich regions such as ultra-faint dwarf galaxies, followed by the transmutation of the host star into a black hole, suppresses the main sequence population in such regions [51, 52].

[v] Neutron star capture of PBHs followed by transmutation of the star into a black hole [53]. However, for this effect to be observable the capture rate must be enhanced by large dark matter densities in nearby regions. Globular clusters may provide one such setting as suggested in Ref. [53], but the dark matter content of these systems is highly uncertain for multiple reasons [54]. In any case, the PBHs are likely to end up in loosely bound orbits around the neutron star and be disrupted by neighbouring stars in dense stellar environments [55].

[vi] PBH transits of white dwarfs may deposit energy via dynamical friction and trigger Type Ia-like supernovae [56], but the heating of nuclear fuel may not occur faster than its cooling by various mechanisms in sizeable portions of the star, making this an unobservable phenomenon for $f_{\text{PBH}} \leq 1$ [21].

-
- [1] B. J. Carr and S. W. Hawking, *MNRAS* **168**, 399 (1974); M. Y. Khlopov, *Res. Astron. Astrophys.* **10**, 495 (2010), arXiv:0801.0116 [astro-ph]; B. Carr, F. Kuhnel, and M. Sandstad, *Phys. Rev. D* **94**, 083504 (2016), arXiv:1607.06077 [astro-ph.CO]; B. Carr and F. Kuhnel, *Ann. Rev. Nucl. Part. Sci.* **70**, 355 (2020), arXiv:2006.02838 [astro-ph.CO].
- [2] A. M. Green and B. J. Kavanagh, *J. Phys. G* **48**, 043001 (2021), arXiv:2007.10722 [astro-ph.CO].
- [3] Y. Bai and N. Orlofsky, *Phys. Rev. D* **99**, 123019 (2019).
- [4] D. Croon, D. McKeen, N. Raj, and Z. Wang, *Phys. Rev. D* **102**, 083021 (2020), arXiv:2007.12697 [astro-ph.CO].
- [5] R. N. Henriksen and L. M. Widrow, *Astrophys. J.* **441**, 70 (1995), arXiv:astro-ph/9402002 [astro-ph].
- [6] M. Fairbairn, D. J. E. Marsh, and J. Quevillon, *Phys. Rev. Lett.* **119**, 021101 (2017), arXiv:1701.04787 [astro-ph.CO].
- [7] N. Blinov, M. J. Dolan, and P. Draper, *Physical Review D* **101** (2020), 10.1103/physrevd.101.035002.
- [8] D. Croon, D. McKeen, and N. Raj, *Phys. Rev. D* **101**, 083013 (2020).
- [9] Y. Bai, A. J. Long, and S. Lu, *JCAP* **09**, 044 (2020), arXiv:2003.13182 [astro-ph.CO].
- [10] A. Ansari, L. Singh Bhandari, and A. M. Thalappillil, *Phys. Rev. D* **109**, 023003 (2024), arXiv:2302.11590 [hep-ph].
- [11] H. Niikura, M. Takada, N. Yasuda, R. H. Lupton, T. Sumi, S. More, T. Kurita, S. Sugiyama, A. More, M. Oguri, and M. Chiba, *Nature Astronomy* **3**, 524–534 (2019).
- [12] N. Smyth, S. Profumo, S. English, T. Jeltema, K. McKinnon, and P. Guhathakurta, *Phys. Rev. D* **101**, 063005 (2020), arXiv:1910.01285 [astro-ph.CO].
- [13] P. S. Ray *et al.* (STROBE-X Science Working Group), (2019), arXiv:1903.03035 [astro-ph.IM].
- [14] C. A. Wilson-Hodge and e. a. Ray, Paul S., in *Space Telescopes and Instrumentation 2016: Ultraviolet to Gamma Ray*, Society of Photo-Optical Instrumentation Engineers (SPIE) Conference Series, Vol. 9905, edited by J.-W. A. den Herder, T. Takahashi, and M. Bautz (2016) p. 99054Y, arXiv:1608.06258 [astro-ph.IM].
- [15] V. Bhalerao *et al.*, arXiv preprint arXiv:2211.12055 (2022); arXiv preprint arXiv:2211.12052 (2022).
- [16] R. Narayan and M. Bartelmann, in *13th Jerusalem Winter School in Theoretical Physics: Formation of Structure in the Universe* (1996) arXiv:astro-ph/9606001.
- [17] T. mpmath development team, *mpmath: a Python library for arbitrary-precision floating-point arithmetic (version*

- 1.3.0) (2023), <http://mpmath.org/>.
- [18] T. T. Nakamura and S. Deguchi, *Prog. Theor. Phys. Suppl.* **133**, 137 (1999).
- [19] N. Matsunaga and K. Yamamoto, *Journal of Cosmology and Astroparticle Physics* **2006**, 023–023 (2006).
- [20] S. Sugiyama, T. Kurita, and M. Takada, *Mon. Not. Roy. Astron. Soc.* **493**, 3632 (2020), [arXiv:1905.06066 \[astro-ph.CO\]](https://arxiv.org/abs/1905.06066).
- [21] P. Montero-Camacho, X. Fang, G. Vasquez, M. Silva, and C. M. Hirata, *JCAP* **08**, 031 (2019), [arXiv:1906.05950 \[astro-ph.CO\]](https://arxiv.org/abs/1906.05950).
- [22] H. J. Witt and S. Mao, *APJ* **430**, 505 (1994).
- [23] J. M. Neilsen, R. C. Hickox, and S. D. Vrtilik, in *American Astronomical Society Meeting Abstracts*, American Astronomical Society Meeting Abstracts, Vol. 205 (2004) p. 102.10.
- [24] “HEASARC tools,” <https://heasarc.gsfc.nasa.gov/ftools/>.
- [25] M. Feroci, M. Ahangarianabhari, G. Ambrosi, F. Ambrosino, A. Argan, M. Barbera, J. Bayer, P. Bellutti, B. Bertucci, G. Bertuccio, *et al.*, in *Space Telescopes and Instrumentation 2018: Ultraviolet to Gamma Ray*, Vol. 10699 (SPIE, 2018) pp. 281–295.
- [26] “SCORPEON Background Model,” https://heasarc.gsfc.nasa.gov/docs/nicer/analysis_threads/scorpeon-overview/.
- [27] J. Klüter, U. Bastian, and J. Wambsganss, *AAP* **640**, A83 (2020), [arXiv:1911.02584 \[astro-ph.IM\]](https://arxiv.org/abs/1911.02584); K. C. Sahu *et al.* (OGLE, MOA, PLANET, μ FUN, MiNDSTeP Consortium, RoboNet), *Astrophys. J.* **933**, 83 (2022), [arXiv:2201.13296 \[astro-ph.SR\]](https://arxiv.org/abs/2201.13296).
- [28] R. W. Hilditch, I. D. Howarth, and T. J. Harries, *MNRAS* **357**, 304 (2005), [arXiv:astro-ph/0411672 \[astro-ph\]](https://arxiv.org/abs/astro-ph/0411672).
- [29] R. M. Ludlam *et al.*, *Astrophys. J.* **927**, 112 (2022), [arXiv:2201.11767 \[astro-ph.HE\]](https://arxiv.org/abs/2201.11767).
- [30] A. Vallenari, A. G. Brown, T. Prusti, J. H. De Bruijne, F. Arenou, C. Babusiaux, M. Biermann, O. L. Creevey, C. Ducourant, D. W. Evans, *et al.*, *Astronomy & Astrophysics* **674**, A1 (2023).
- [31] R. Lin, M. H. van Kerkwijk, F. Kirsten, U.-L. Pen, and A. T. Deller, *APJ* **952**, 161 (2023), [arXiv:2306.01617 \[astro-ph.HE\]](https://arxiv.org/abs/2306.01617).
- [32] “HEASARC tools,” https://heasarc.gsfc.nasa.gov/docs/nicer/nicer_archive.html.
- [33] K. Griest, *APJ* **366**, 412 (1991).
- [34] X. Ou, A.-C. Eilers, L. Necib, and A. Frebel, *MNRAS* **528**, 693 (2024), [arXiv:2303.12838 \[astro-ph.GA\]](https://arxiv.org/abs/2303.12838).
- [35] Y. Jiao, F. Hammer, H. Wang, J. Wang, P. Amram, L. Chemin, and Y. Yang, *Astron. Astrophys.* **678**, A208 (2023), [arXiv:2309.00048 \[astro-ph.GA\]](https://arxiv.org/abs/2309.00048).
- [36] C. Roche, L. Necib, T. Lin, X. Ou, and T. Nguyen, *arXiv e-prints*, [arXiv:2402.00108](https://arxiv.org/abs/2402.00108) (2024), [arXiv:2402.00108 \[astro-ph.GA\]](https://arxiv.org/abs/2402.00108).
- [37] X. X. Xue *et al.* (SDSS), *Astrophys. J.* **684**, 1143 (2008), [arXiv:0801.1232 \[astro-ph\]](https://arxiv.org/abs/0801.1232).
- [38] J. S. Deneva *et al.*, *Astrophys. J.* **874**, 160 (2019), [arXiv:1902.07130 \[astro-ph.HE\]](https://arxiv.org/abs/1902.07130).
- [39] A. K. Harding and C. Kalapotharakos, *arXiv preprint arXiv:1712.02406* (2017).
- [40] M. Crispim Romão and D. Croon, (2024), [arXiv:2402.00107 \[astro-ph.CO\]](https://arxiv.org/abs/2402.00107).
- [41] B. V. Lehmann, S. Profumo, and J. Yant, *JCAP* **04**, 007 (2018), [arXiv:1801.00808 \[astro-ph.CO\]](https://arxiv.org/abs/1801.00808); M. Gorton and A. M. Green, (2024), [arXiv:2403.03839 \[astro-ph.CO\]](https://arxiv.org/abs/2403.03839).
- [42] G. Dvali, L. Eisemann, M. Michel, and S. Zell, *Phys. Rev. D* **102**, 103523 (2020), [arXiv:2006.00011 \[hep-th\]](https://arxiv.org/abs/2006.00011).
- [43] A. Alexandre, G. Dvali, and E. Koutsangelas, (2024), [arXiv:2402.14069 \[hep-ph\]](https://arxiv.org/abs/2402.14069).
- [44] V. Thoss, A. Burkert, and K. Kohri, (2024), [arXiv:2402.17823 \[astro-ph.CO\]](https://arxiv.org/abs/2402.17823); G. Dvali, J. S. Valbuena-Bermúdez, and M. Zantedeschi, (2024), [arXiv:2405.13117 \[hep-th\]](https://arxiv.org/abs/2405.13117).
- [45] D. A. Smith *et al.* (Fermi-LAT), *Astrophys. J.* **958**, 191 (2023), [arXiv:2307.11132 \[astro-ph.HE\]](https://arxiv.org/abs/2307.11132).
- [46] R. Takahashi and T. Nakamura, *The Astrophysical Journal* **595**, 1039–1051 (2003).
- [47] A. Katz, J. Kopp, S. Sibiryakov, and W. Xue, *JCAP* **12**, 005 (2018), [arXiv:1807.11495 \[astro-ph.CO\]](https://arxiv.org/abs/1807.11495).
- [48] R. J. Nemiroff and A. Gould, *APJL* **452**, L111 (1995), [arXiv:astro-ph/9505019 \[astro-ph\]](https://arxiv.org/abs/astro-ph/9505019); R. J. Nemiroff, *APSS* **259**, 309 (1998), [arXiv:astro-ph/9806012 \[astro-ph\]](https://arxiv.org/abs/astro-ph/9806012).
- [49] P. Gawade, S. More, and V. Bhalerao, *Mon. Not. Roy. Astron. Soc.* **527**, 3306 (2023), [arXiv:2308.01775 \[astro-ph.CO\]](https://arxiv.org/abs/2308.01775).
- [50] T. X. Tran, S. R. Geller, B. V. Lehmann, and D. I. Kaiser, (2023), [arXiv:2312.17217 \[astro-ph.CO\]](https://arxiv.org/abs/2312.17217).
- [51] N. Esser and P. Tinyakov, *Phys. Rev. D* **107**, 103052 (2023), [arXiv:2207.07412 \[astro-ph.HE\]](https://arxiv.org/abs/2207.07412).
- [52] N. Esser, S. De Rijcke, and P. Tinyakov, *Mon. Not. Roy. Astron. Soc.* **529**, 32 (2024), [arXiv:2311.12658 \[astro-ph.GA\]](https://arxiv.org/abs/2311.12658).
- [53] F. Capela, M. Pshirkov, and P. Tinyakov, *Phys. Rev. D* **87**, 123524 (2013), [arXiv:1301.4984 \[astro-ph.CO\]](https://arxiv.org/abs/1301.4984).
- [54] R. Garani, N. Raj, and J. Reynoso-Cordova, *JCAP* **07**, 038 (2023), [arXiv:2303.18009 \[astro-ph.HE\]](https://arxiv.org/abs/2303.18009).
- [55] R. Caiozzo, G. Bertone, and F. Kühnel, (2024), [arXiv:2404.08057 \[astro-ph.HE\]](https://arxiv.org/abs/2404.08057).
- [56] P. W. Graham, S. Rajendran, and J. Varela, *Phys. Rev. D* **92**, 063007 (2015), [arXiv:1505.04444 \[hep-ph\]](https://arxiv.org/abs/1505.04444).